Failure Mechanisms in Flip-Chip Bonding on Stretchable Printed Electronics

Mohammad H. Behfar, Behnam Khorramdel, Arttu Korhonen, Elina Jansson, Aleksis Leinonen, Markus Tuomikoski, and Matti Mäntysalo**

Accelerating progress in printed electronics technology transforms the future of the manufacturing process in industrial applications, consumer electronics, and healthcare products. However, real-life applications demand for circuits and systems that are robust and can stay functional under strong and frequent mechanical deformations. Herein, both empirical and analytical approaches to gain insight on the reliability of ultrathin bare dies on soft and highly stretchable printed circuits are used. To this end, a set of conductive ink and adhesive variants are used to develop a stretchable wireless temperature logger as the test device. The electromechanical performance of the conductive inks is first verified through the screening tests and the most suitable candidates are selected to use with different anisotropic conductive adhesives (ACAs) for chip bonding process. The performance of the test devices (per ink–adhesive combination) is tested through cyclic elongation of 60 samples to provide statistical results. Different failure modes are visualized through cross-sectional images using broad ion beam (BIB) milling and scanning electron microscopy (SEM). The findings, herein, recognize pad delamination, air voids at the chip-to-substrate interface, stiffness of the conductive adhesives, and bonding parameters (pressure and temperature) as the key contributors to the contact failures in the chip assembly.

1. Introduction

Growing advances in printed flexible electronics enable novel design and manufacturing processes of electrical circuits and components in aircraft and automotive industries,[1–3] as well as in consumer electronics for fabrication of printed passive components, semiconductor devices, and sensing elements.[4–15] In the
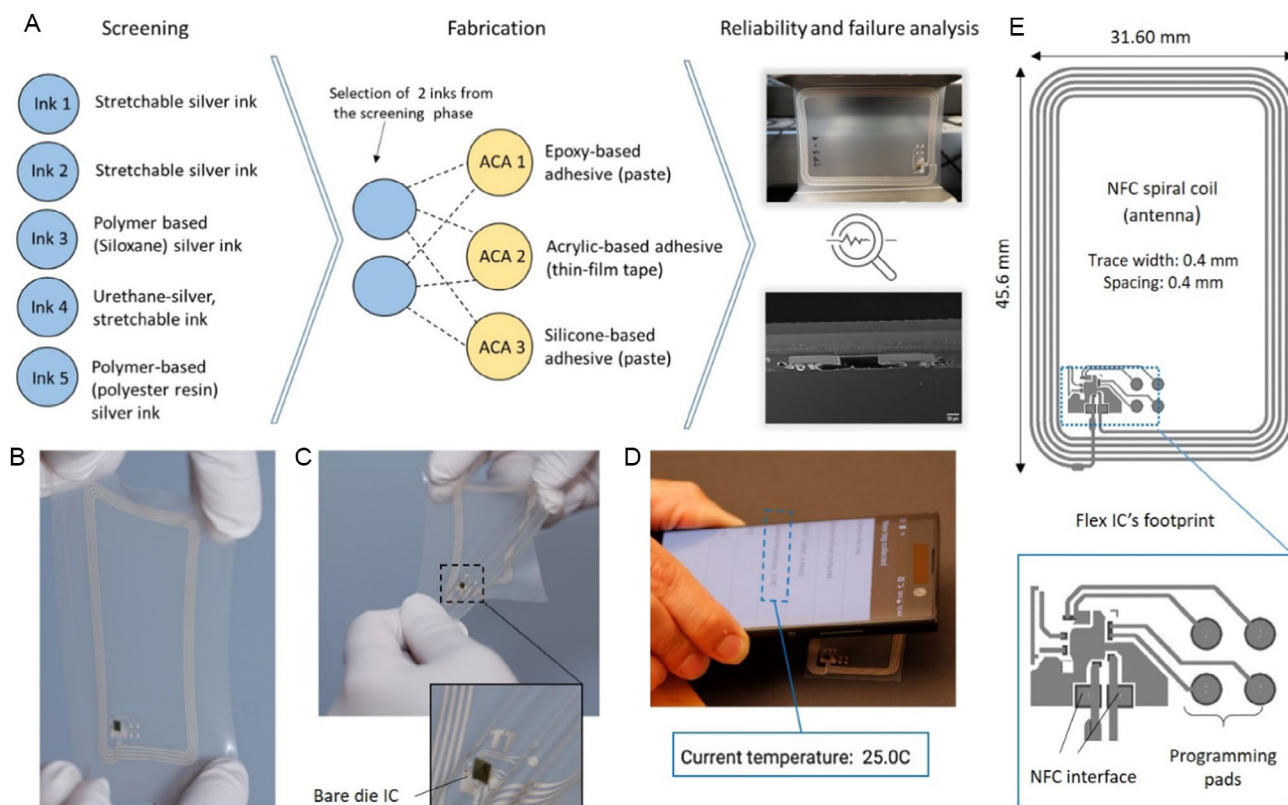
M. H. Behfar, A. Korhonen, E. Jansson, M. Tuomikoski
VTT Research Center of Finland
Oulu 90570, Finland
E-mail: mohammadhossein.behfar@vtt.fi

B. Khorramdel, A. Leinonen, M. Mäntysalo
Faculty of Information Technology and Communication Sciences
Tampere University
33720 Tampere, Finland
E-mail: matti.mantysalo@tuni.fi

The ORCID identification number(s) for the author(s) of this article can be found under https://doi.org/10.1002/adem.202100264.

healthcare domain, the impact of printed electronics becomes more profound and offers a wide range of applications from printed RF coils for medical imaging,[16] biochemical sensing,[17,18] vital sign monitoring[19–25] to assistive wearable devices.[26,27] At the industrial level, its low cost and high-throughput manufacturing process are the key motivators for transition from conventional solutions to printed technologies. In wearable applications, its capability to realize soft wearable sensors, which can comply with the dynamic deformations of human skin, is attractive.

Despite the promising opportunities of printed electronics in different domains, there are concerns regarding the reliability of printed materials (i.e., conductive inks, isolators, and adhesives) and their interconnections to electronic components for long-term use in real-life applications. Over the past decade, there has been an increasing number of studies on the reliability of printed conductors, interconnections, and chip-on-flex assembly. As a fundamental test, the cyclic bending endurance of printed conductors was investigated to analyze the characteristics of conductive tracks on a flexible substrate.[28–30] In more complicated test protocols, the influence of environmental parameters (e.g., temperature, humidity, etc.) was included in the test procedure.[31] More advanced test setups and protocols were developed to evaluate the reliability of complex hybrid integration of chip-on-flex, flex-to-flex assemblies, and roll-to-roll (R2R) printed circuits.[32–34]

This work presents a comprehensive study on the reliability of hybrid integration of thinned bare die chip on soft and stretchable substrate. More specifically, the findings of this study are expected to provide fundamental insights on the failure mechanisms, their corresponding contributors, and ways to minimize them. This study is divided into three phases as shown in **Figure** 1A. In the screening phase, the electromechanical performance of five different ink variants is evaluated and the most suitable ink variants are selected to be used in combination with three different types of conductive adhesive for fabrication and assembly of the test device. In the last phase of the study, the fabricated test devices are tested through a cyclic strain test and a comprehensive analysis of failure mechanisms is performed. The importance of the failure analysis is recognized in refining of the design steps, material selection, and processing parameters for improved reliability.

ADVANCED
SCIENCE NEWS
www.advancedsciencenews.com

ADVANCED
ENGINEERING
MATERIALS
www.aem-journal.com

Figure 1. A) Study flow diagram. B,C) Elastic temperature logger. D) Temperature measurement with the test device using a NFC-enabled mobile phone. E) Layout of the test device circuitry.

The test device for this study is a stretchable wireless temperature logger, which comprises a bare die near-field communication (NFC) tag and a printed spiral inductor (Figure 1B,C). The temperature logger was fabricated on a thin (100 μm), highly stretchable thermoplastic polyurethane (TPU) substrate. The layout and geometry of the spiral inductor are based on a standard NFC antenna, which operates at regulated NFC frequency (Figure 1D). The conventional rigid integrated circuits (ICs) restrict bending, twisting, and deformation of flexible electronics assembly.[35] To overcome this issue, this study utilizes a commercial flexible, thinned (40 μm) bare die chip with 10 μm Ni/Au-plated bond pads (AS_NHS3100P). The test device's mechanical properties such as softness, stretchability, and conformity resemble a typical wearable skin patch, and therefore, the reliability test criteria are set to emulate real-life conditions. The human skin is limited to a maximum strain of approximately 30%.[36] However, the strain of human skin during normal operations is found to be less than 20%.[37] Based on the given numbers, the upper limit for cyclic strain of the test device was set to 20% up to 5000 cycles. The test device's layout topology is divided into the NFC antenna and the flex IC's footprint. This division facilitates the analysis of different modes of failure. For instance, when the interconnections between the layout and IC's pad are stable, any failure in wireless (NFC) operation can be attributed to the failure of conductive ink in the antenna layout. It should be noted that both electromagnetic and temperature sensing performance of the device stay beyond the scope of this work, as this study focuses on the durability of the interconnections and the source of the failures.

All the printing and assembly processes of the test device were designed to be compatible with high-throughput manufacturing methods such as automated sheet-to-sheet and roll-to-roll processing. Roll-to-roll printing and component assembly offer the advantages of large-scale and low-cost manufacturing. Moreover, leaner logistics and value chains with less material loss and fewer mechanical parts result in environmentally friendly products.

2. Results and Discussion

2.1. Ink Stretchability, Single Pull Versus Cyclic Performance

In the screening phase, all the stretchable conductive tracks were fabricated by rotary-screen through a roll-to-roll (R2R) process using five ink variants. **Table 1** presents the specification of the ink variants used in this study and a graphical illustration of R2R process is shown in **Figure 2**A. The ink variants are all silver flake inks as they are known for relatively high elongation tolerance while maintaining low sheet resistance. The conductive tracks were printed on a 100 μm-thick TPU substrate. A removable PET carrier film was attached on the backside of the substrate to improve the mechanical stability during the R2R printing process. Following the printing, all the inks were annealed in the hot air oven of the R2R line at 140 °C. Based on the resistance measurement, Ink1 possesses the highest sheet resistance whereas all the other ink variants have relatively lower sheet resistance, which qualifies them for NFC application.

Table 1. Specification of the ink variants used in this study.

Ink	Type	Part number	Average Sheet resistance [$m\Omega\ sq^{-1}$]	Min.	Max.
Ink 1	Stretchable silver flake ink	Creative Materials 127-48	1220	1098	1304
Ink 2	Stretchable silver flake ink	Dupont PE-874	200	183	206
Ink 3	Polymer-based (siloxane) silver flake ink	Inkron IPC-500	163	141	187
Ink 4	Urethane-based silver flake ink	ECM CI-1036	51	48	56
Ink 5	Polymer-based (polyester resin) silver flake ink	Asahi LS-411AW	65	57	71

Electromechanical performance of the different inks on TPU substrate was investigated using a uniaxial testing device in a single-pull and cyclic loading conditions. The geometry of the conductive track was a U-shaped line with connector pads at one side to measure the resistance (Figure 2B). The connector side is attached to the static end of the uniaxial stretching device while the other end is moving during the uniaxial stretch test (Figure 2C). This arrangement limits the unwanted movement of measurement cables to minimize electrical noise. In the single-pull test, conductive tracks were stretched up to a pre-defined electrical breakpoint (100 MΩ), where they lost the conductance. Figure 2D shows the normalized resistance of the inks as a function of the applied strain. Normalization was done by dividing the resistance at a given strain over the resistance value at zero strain. As can be seen from the graphs, the ink resistivity started to increase linearly at lower strain but exponentially at higher strain up to the point where they reached the electrical breakpoint.

The electrical breakpoint of each ink versus the applied strain is shown in Figure 2E. The breakpoints for Ink1 and Ink5 were found to be less than 30%, while all the other inks survived more than 60% of elongation. Following the single-pull strain test, the cyclic strain tests were performed to ensure the durability of the inks over repeated elongation. All the samples were stretched 1000 cycles at the speed of 200 mm min^{-1}. The cyclic test was first performed with 10% for all samples and then 20% for the selected inks. As shown in Figure 2F, only Ink2 and Ink4 survived 1000 cycles at 10%, and therefore, only those two inks were tested for cyclic 20% elongation (Figure 2G,H). The inks' strain–resistance characteristic curves note that the single-pull performance of the inks does not necessarily correlate with the results of cyclic tests. For instance, Ink2 survived best in the single-pull test whereas it approached the failure threshold in the cyclic test (at 20% strain) after 200 cycles. In contrast, Ink4 survived 500 cycles at 20% cyclic loading, while it tolerated less strain before reaching the breakpoint in a single-pull test compared to Ink2. Furthermore, it is important to notice the difference in the performance of these inks over the continuous cyclic strain and how it is reflected in the results. The resistance of Ink4 increased during the cyclic stretching and eventually

reached the pre-set failure threshold after 500 cycles (at 20% strain); however, the ink resistance returned to a lower value when the applied stress was zero at the end of each cycle. This minimum resistance at each cycle increased linearly. This time-dependent recovery is likely caused by intrinsic structural properties of the ink and the TPU substrate. In the case of Ink2, the increase of minimum resistance was exponential, which means that the conductive track did not recover after each cycle, and the conductivity of the printed line degraded at each cycle until it reached the failure threshold.

The ink screening study solely focused on the electromechanical performance of the inks and suggested that Ink2 and Ink4 performed best in their cyclic elongation tests. Therefore, they were selected for printing of the test devices (NFC tags).

2.2. Reliability and Analysis of Failure

2.2.1. System Level Reliability

The NFC tags were fabricated through a sheet-to-sheet process (**Figure 3**A) using six variants of ink–adhesive combinations; two inks (Ink2 and Ink4) selected from the screening phase and three conductive adhesive variants. **Table 2** presents the specification of the conductive adhesives used in the bonding process. To statistically analyze the results, ten samples per ink–adhesive combination were tested through cyclic uniaxial 20% strain at 20 mm min^{-1} as shown in Figure 3C. The only exception is ACA3–Ink2 combination where one of the samples failed before the test. In the test protocol, the tag is considered functional if all the IC's pad-to-footprint interconnects are connected and the tag can be detected by an external reader when the sample is not under strain and the substrate is relaxed. Testing the devices in their relaxed status ensures that the NFC antenna has the minimum resistance for wireless operation. The system failure can be a result of failure in the silver ink or failed interconnection. For the test device, the NFC operation only requires a functional NFC antenna and a stable connection to the IC's antenna input pins. Thus, the ink failure in NFC operation is confirmed when the antenna pins are connected to the antenna layout, but the NFC operation does not function. This indicates that the spiral antenna has failed due to a mistuned or high impedance coil. The status of IC's pad-to-footprint interconnection is checked by testing the internal protection diode of IC's individual pins using a multimeter as described in the supplementary information (Figure S1, Supporting Information).

Figure 3B presents the outcome of the 20% cyclic strain test, indicating that the samples printed with Ink4 and assembled with ACA1 could considerably last longer compared to the samples fabricated with other combinations of materials used in this study. With this combination, all the samples could survive at least 3500 cycles and 70% of total samples stayed functional at 5000 cycles of 20% elongation. In the second position, the combination of the same adhesive and Ink2 performed best. However, there is a significant drop in the survival of the samples over the cyclic strain. In this case, only one sample could stay functional until 3000 cycles and 60% of the samples last less than 2000 cycles. As shown in Figure 3C, all the failures in the combination of ACA1–Ink4 are attributed to the interconnection failure whereas in the case of ACA1–Ink2, 80% of the failure relates
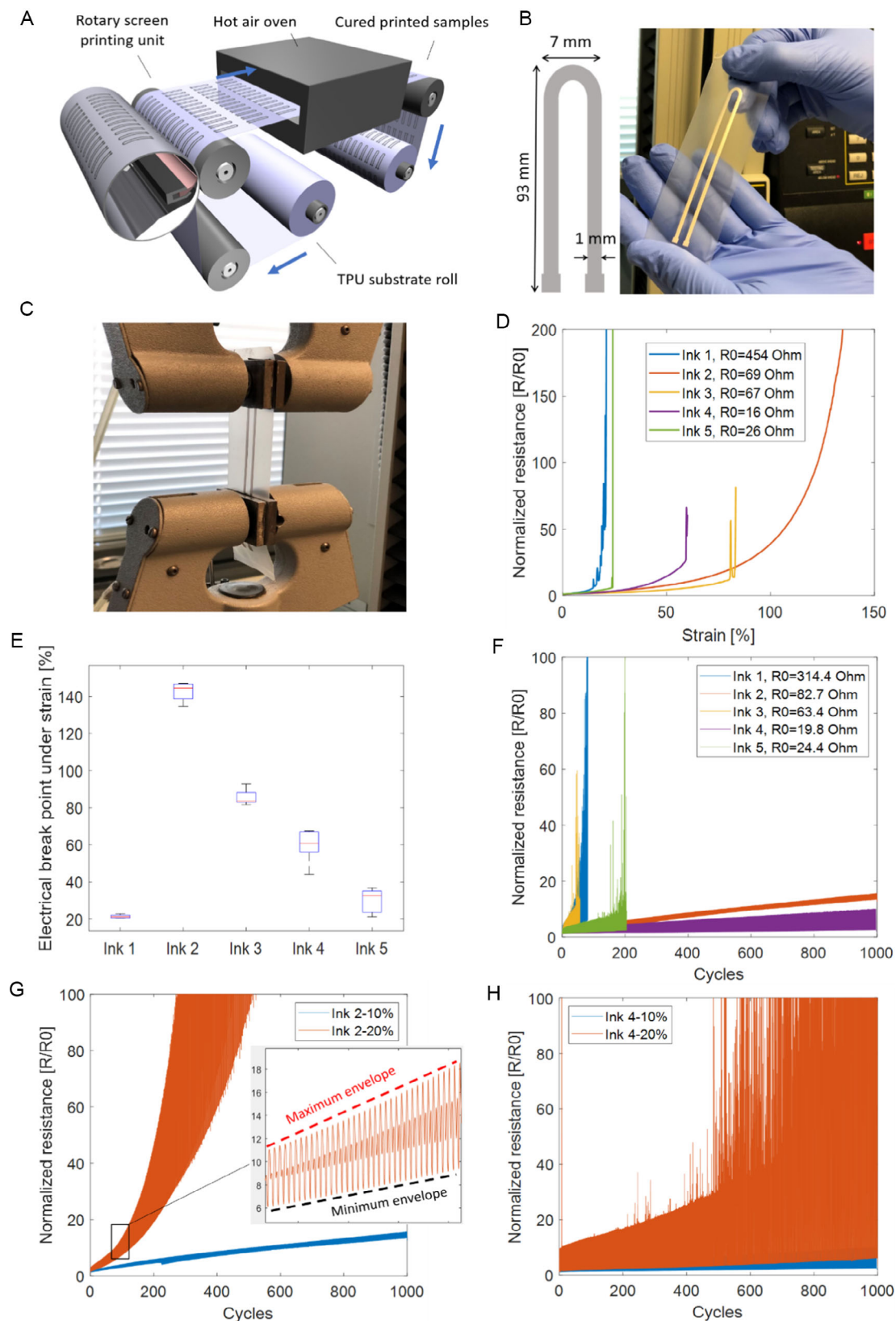
Figure 2. A) Graphical illustration of the R2R printing process. B) U-shaped connector used in the screening phase. C) Uniaxial single-pull strain test setup. D) Change in resistance as a function of elongation in the single-pull test. E) Electrical breakpoint of different inks versus applied strain. F) Resistance change of all inks in the 10% cyclic test. G) Resistance change of Ink2 in the cyclic test with 10% and 20% elongation. H) Resistance change of Ink4 in the cyclic test with 10% and 20% elongation.
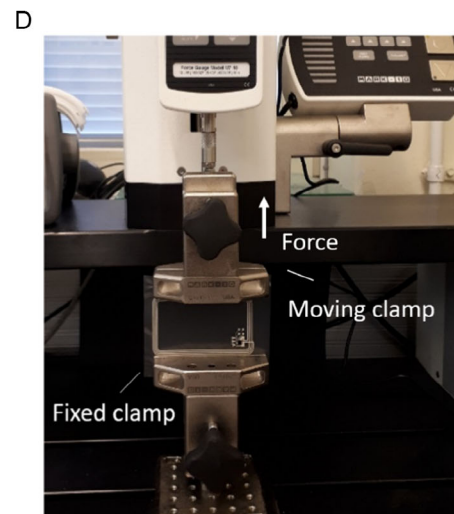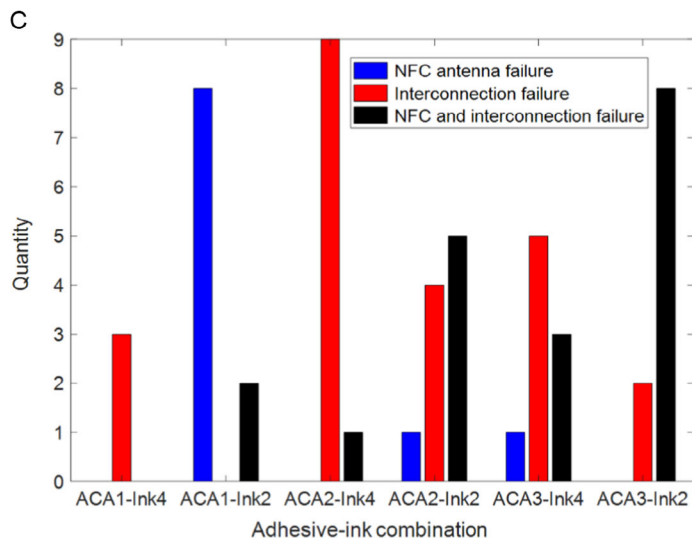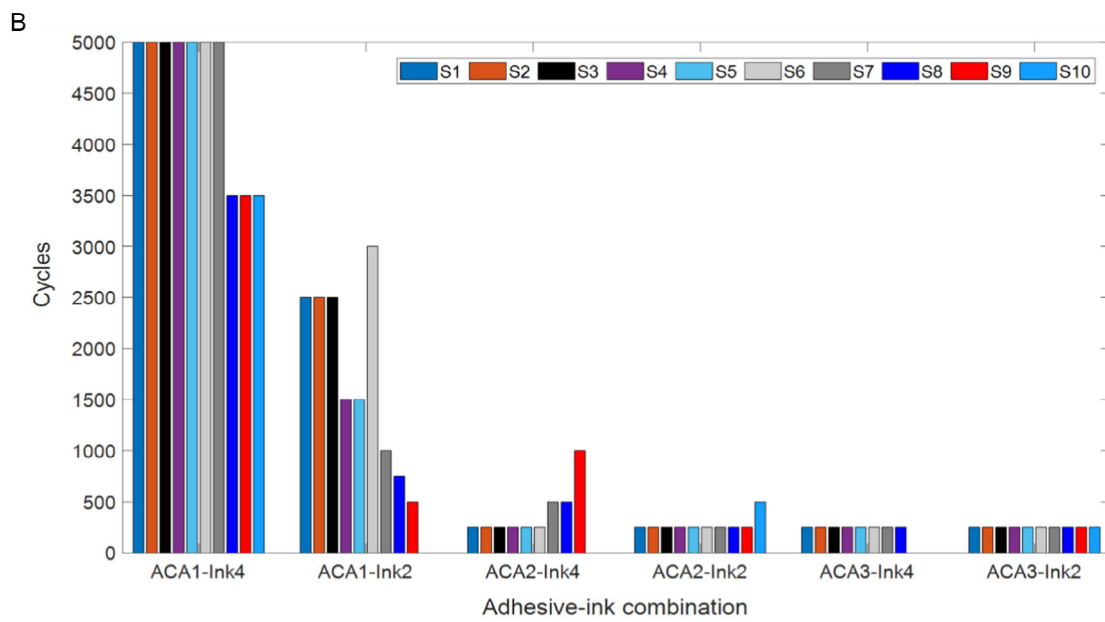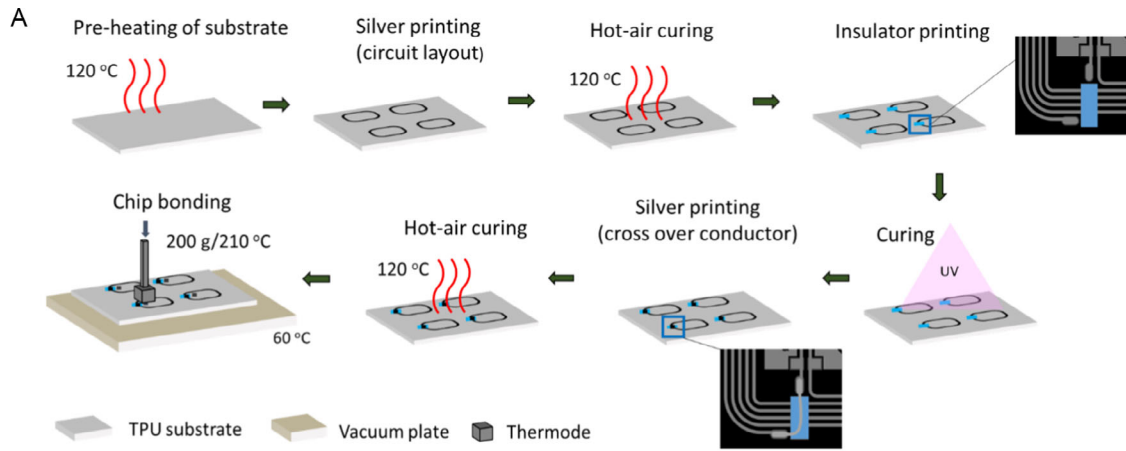
Figure 3. A) Graphical illustration of the sheet-to-sheet fabrication process of the test device. B) Results of the 20% cyclic strain test of the test devices (per ink–adhesive combination). C) Confirmed cases of ink failure versus interconnection failure. D) Cyclic uniaxial 20% strain test setup.

ADVANCED
SCIENCE NEWS
www.advancedsciencenews.com

ADVANCED
ENGINEERING
MATERIALS
www.aem-journal.com

Table 2. Electrically conductive adhesives used in the study.

Conductive adhesive	Type	Part number	Modulus [MPa]
ACA1	Epoxy-based paste adhesive	Delo AC245	3900
ACA 2	Thin film (10 µm), acrylic-based conductive transfer adhesive	Tesa 60 581	N/A
ACA 3	Silicone-based paste adhesive	Creative Materials EXP 2647-57-2	0.2

to ink failure and 20% is attributed to both ink and interconnection failure. This can be explained by a different performance of the inks as discussed in the previous section. It has been observed that the conductance of Ink2 degrades exponentially (without quick conductance recovery) as a function of cycles of strain.

Ink2 and Ink4 were also used with ACA2 and ACA3; however, those tolerated significantly fewer cycles of strain compared to the devices assembled with the epoxy-based adhesive (ACA1). The information given by the graphs in Figure 3B suggests that the impact of the conductive adhesive is dominant in the tolerance of samples to cyclic strain. The epoxy-based adhesive (ACA1) has a considerably higher Young's modulus than the acrylic-based film (ACA2) and silicone-based (ACA3) adhesives. This indicates that Young's modulus of the conductive adhesives is the key contributor to the reliability of the interconnection. In practice, an ACA with higher Young's modulus could resist more effectively against the mechanical stress imposed on the chip-to-substrate interface during the cyclic strain; and therefore, the interconnections can tolerate higher cycles of stretching compared to the samples assembled using the adhesives with lower Young's modulus. This is important especially in the case of conductive adhesives with micrometer-sized particles where even slight deformation in ACA matrix leads to loss of conductive
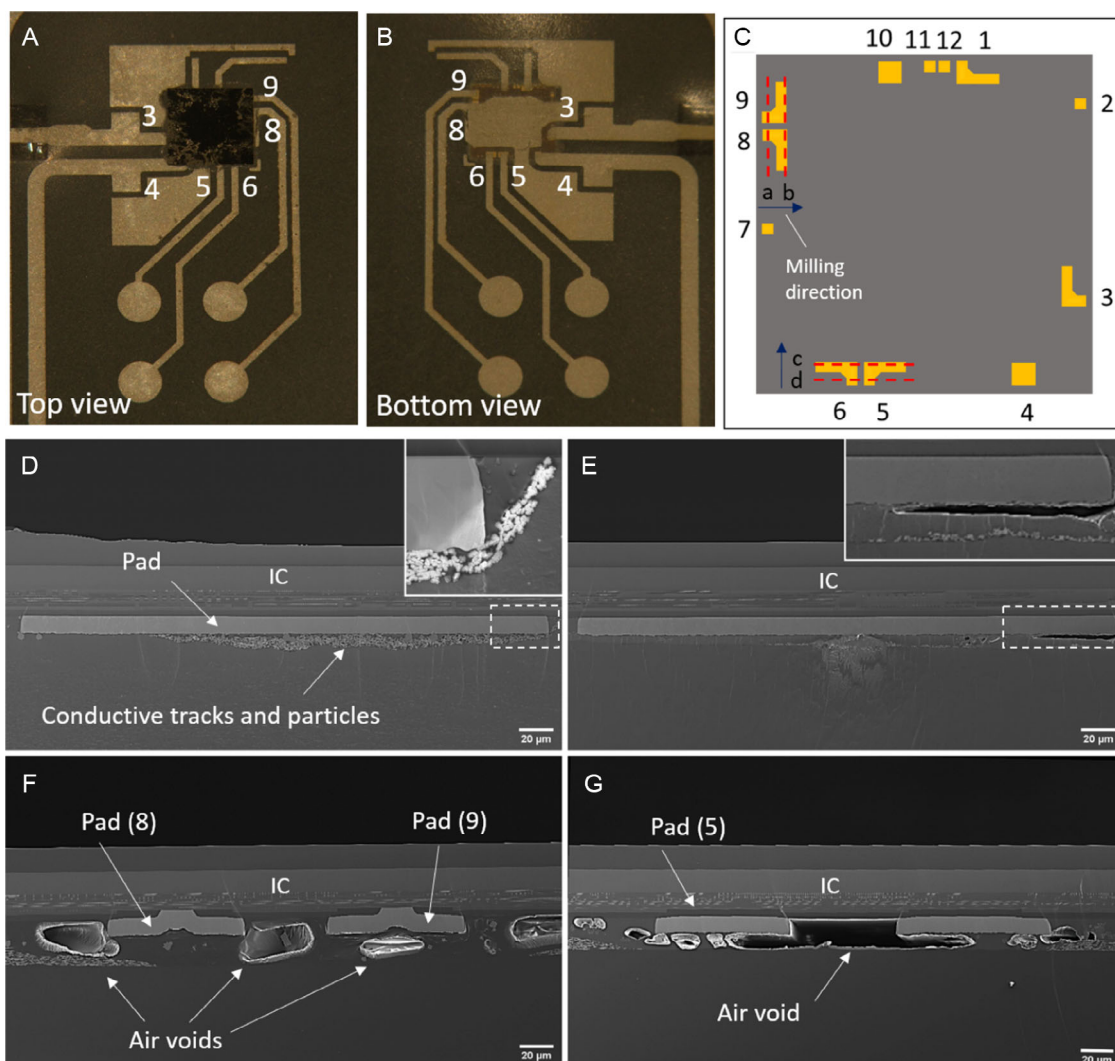
Figure 4. A,B) Top and bottom views of the assembled chip with marked connections. C) Schematic picture of chip's contact pads. D) SEM micrograph of the failure caused by overpenetration of the pad to the substrate. E) SEM micrograph of the failure caused by delamination of the pad. F,G) SEM micrographs of the failures caused by air voids.

path. A detailed analysis of the scenarios where the interconnections failed in this study is given in the following section.

2.2.2. Analysis of Failures

Figure 4A,B show, respectively, the top view and bottom view of the bonded chip with marked connections. Figure 4C presents the layout of the chip contact pads as well as the cross sections made for the SEM imaging. The following reports the main failures categorized in three cases observed through cross-sectional imaging.

Over-Penetrated Pad: This failure happened with ACA1–Ink2 combination as shown in Figure 4D. In this case, connection 6 (cross section "c" in Figure 4C) failed early during the stretching test. This could be explained by penetration of the chip's pad to the substrate and conductive track (magnified in the inset) because of possible excessive bonding pressure and temperature. This could cause potential weak (i.e., break) points as we see in the right edge of failed pad-to-footprint connection.

Delamination: This failure happened with ACA3–Ink2 combination as shown in Figure 4E. In this case, connection 9 (cross section "b" in Figure 4C) failed. This could be because of the fact that, at least at this specific depth of the cross section, no visible connection can be observed between the conductive track and the pad. Also, mechanical stress from the stretching and cyclic loading has caused delamination (magnified in the inset) which weakens the strength of the interconnection, increases the distance between the chip and substrate, and causes failure. Other than the mechanical stresses, poor adhesion could also result in delamination because of the incompatibility of the polymer with the substrate, substrate contamination, or moisture ingress to the polymer. In the case of delamination, adhesive particles cannot create any electrical connection.

Air Voids: This failure happened with ACA2–Ink4 combination as shown in Figure 4F. In this case, connection 9 (cross section "a" in Figure 4C) failed. At this depth of the cross section, there is an air void under the pad. This void decreases the strength of the adhesive and finally breaks the electrical connection by making a gap between the pad and conductive track because of the absence of conductive particles. At the same depth (cross section "a"), connection 8 shows no connection because of two large air voids at the corners of the pad. However, the connection remained functional because of the possible connection of conductive particles to the conductive track at some further depth without the voids. As can be seen, the voids could be mostly trapped at the corner of the pads. This type of failure was also found in ACA3–Ink4 combination as shown in Figure 4G. Here, connection 5 (cross section "d" in Figure 4C) failed. The failure is the result of the expanded air voids during the cyclic stretch around the pad, which caused a severe gap between the pad and substrate. That failure is marked "Air void" in Figure 4G.

The air voids could be formed by improper (too quick) curing of the adhesive with higher temperatures during the bonding step.[38,39] In fact, high heating rate can cause disruption in the flow of the conductive adhesive matrix. Moreover, inadequate amount of adhesive for filling the whole volume (pad-to-substrate gap) could be also a reason for the formation of the air voids. It is also worth noting that lower Young's modulus of the cured adhesives could potentially cause expansion of the voids under cyclic stretching conditions. The expanded voids increase the gap between the pads and conductive tracks, which results in broken electrical contact. To ensure the maximum stiffness of the conductive adhesive, in the chip bonding process, the bonding force should be kept until the adhesive is fully cured as recommended by the manufacturer.[40]

3. Conclusion

This study analyzed the failure mechanisms and discussed the impact of mechanical properties of the conductive adhesives, chip bonding force, curing time, and amount of dispensed conductive adhesive on the reliability of the interconnections. The observations from this study recognized the formation of the air voids as the key contributor to the failure cases. In case of failure with the air voids, the failure procedure starts by the formation of voids at the chip-to-substrate interface, then proceeds to the expansion of the voids during cyclic strain all over the interface and finally causes permanent delamination. The creation of the void can be related to multiple intrinsic and process-dependent parameters. The voids can be created as the result of high-temperature pre-bonding treatment, amount of the adhesive, curing time, as well as Young's modulus of the adhesive matrix. Moreover, it has been observed that excessive bonding force during the assembly process could impose mechanical stress on the pad-to-footprint interface and create potential weak points for failure.

The concept of reliability depends on the target application and varies from case to case. However, gaining fundamental insights on the mechanism of failure can facilitate optimization of the integration process to achieve the desired level of reliability and system integrity. The observations from the cyclic stretch test of the devices indicate that an acceptable level of reliability can be realized by proper selection of materials and optimum integration process. As discussed earlier, ACA1 has the highest Young's modulus among the other ACAs used in this study. The experimental analysis of failures suggests that the ACA with higher Young's modulus could maintain the distance between the chip's pad and the substrate more effectively. Considering the micronsized conductive particles of ACAs, the improved mechanical stability secures an electrical connection between the pad and printed layout on the substrate. It has been demonstrated that the devices fabricated with ACA1–Ink4 combination could tolerate 5000 cycles of 20% elongation, which is sufficient for applications such as wearable sensors and skin patch devices.

4. Experimental Section

Roll-to-Roll Printing of the U-Shaped Conductor Tracks: The U-shaped silver conductor lines were rotary screen printed with roll-to-roll (R2R) production line on a 100 μm-thick TPU substrate. To ensure a proper runnability of the TPU substrate in the continuous R2R process under web tension, a thin removable PET carrier foil was added on the backside of the substrate before the printing. In addition, the TPU substrate was pre-treated in the hot air ovens of the production line at 140 °C to minimize the dimensional changes of the substrate during the printing. The pretreatment speed was set to 2 m min⁻¹. Five different ink variants were

used to print the conductors as presented in Table 1. For all the inks (except Ink3), a screen with a mesh count of 305 lines inch^{-1} was used and the printing speed was set to 2 m min^{-1}. Ink3 differed from the other inks because of solid content above 95%, and thus, a coarser screen with a lower mesh count of 215 lines inch^{-1} and a lower printing speed of 1 m min^{-1} were used for the printing process. All the printed ink layers were dried at 140 °C, which is the maximum temperature of the ovens of the R2R line used in this study. In R2R printing, the drying time is often short because of the limited oven length and constantly moving web. The optimum drying conditions for the given inks vary from 100 °C for 10 min to 150 °C for 20 min; however, it is not possible to apply these long drying times in the R2R line. Therefore, a temperature of 140 °C was used to ensure proper drying of the ink layer by setting the highest possible temperature together with the lowest printing speed.

Sheet-to-Sheet Printing of NFC Temperature Logger: NFC antennas were printed onto the same type of TPU substrate (as used in the R2R printing) using an automatic sheet-to-sheet printer. The printed antenna structure consists of four layers: an antenna coil, two insulator layers, and a cross-over conductor. The mesh count of the screen was 400 lines in.$^{-1}$ for the antenna coil and 325 lines in.$^{-1}$ for the other layers. The substrate was pretreated in a hot-air oven at 120 °C before the printings to prevent dimensional changes of the substrate during printing, thus ensuring proper registration accuracy in this multilayer approach. The substrate was used without any carrier foils. The layout of the NFC temperature logger was printed with two ink variants (Ink2 and Ink4). The printed silver layers were dried in a hot-air oven at 120 °C after the printings. The same drying and printing conditions were used for both silver inks. The insulator layers were printed with clear UV-curable ink. Two layers of insulators were printed to ensure reliable insulation between the silver layers. The UV curing power and time were, respectively, set to 1000 W and 30 s for both of the insulator layers. The same printing and curing conditions were used for cross-over silver printing on the top of the insulator layer.

Chip Bonding and Assembly: Chip assembly was carried out using a high-accuracy, multichip die bonder (Datacon 2200 EVO). The bonding of the chips was performed using three different ACAs as presented in Table 2. The chips bonded with ACA1 and ACA3 were thermo-compressed (weight: 200 g) at 210 and 230 °C for 40 s, respectively. The temperature of the vacuum plate underneath the chip and TPU substrate was set to 60 and 80 °C for ACA1 and ACA3, respectively. In addition, in the chip assembly process with ACA1 and ACA3, a protection tape between the chip and bonding tool was utilized during the thermo-compression. In the case of ACA2, the adhesive film was manually applied between the chip and substrate, and then thermo-compressed (weight: 250 g) at 60 °C for 10 s. The temperature of the vacuum plate underneath the chip and TPU substrate was set to 60 °C.

Single-Pull and Cyclic Stretching of the Ink: A set of eight samples (five for single-pull stretching and three for cyclic strain) per ink variant was used for the characterization. First, all the fabricated samples were checked visually to ensure that there were no visible defects in the conductive tracks. Later, five samples per ink variant were stretched in one direction by a tensile tester (Instron 4411 universal Testing Machine) up to the pre-defined electrical breakpoint (100 MΩ). A customized clamping system with a thin layer of rubber was used to provide enough grip on the samples during the test. To avoid damaging the conductive tracks caused by the clamps, some grooves were made on the rubber surfaces. In this setup, pads were placed below the fixed clamps to avoid the measurement noise during the electromechanical characterization. A 500 N load cell was used to pull the samples at the speed of 20 mm min^{-1}. Simultaneously, the DC resistance of the samples was measured using a Keithley 2425 multimeter with a sampling rate of 5 Hz, which was controlled by a customized LabVIEW software. More details about the test setup are given in a previous study.[41]

With another test setup, the long-life performance of the samples was evaluated by repetitive stretching–releasing cycles using the same tensile tester machine. In this setup, the test speed was set to 200 mm min^{-1}, and three samples were stretched (grip distance: 50 mm) by 10% and 20% for 1000 cycles.

Temperature Logger Cyclic Strain: The NFC tags were tested through a specified test protocol using a PC-controlled tensile tester (Mark-10). The test protocol regulated vertical, uniaxial cyclic stretching of the samples at 20% elongation with the speed of 200 mm min^{-1} up to 5000 cycles. For the first 1000 cycles, the test break interval was set to 250 cycles. At each break interval, the stretch test stopped, and electrical function of the samples was fully inspected as described earlier. From cycle 1001 onward, the break interval was set to 500, and the same inspection procedure was repeated.

RFID System Verification: The performance of the NFC operation was evaluated using a companion mobile application. The connectivity of the programming and power pads (pad-to-footprint connectivity) were also checked using a multimeter by testing the internal protection diode of the IC's pins. If the NFC tag was identified by the phone and also all the chip's contact pads were connected to the footprint on the substrate, then the sample was labeled as "passed sample" and the test continued to the next step. The procedure was repeated up to the point where a sample failed or the stretching counter reached 5000 cycles.

Interconnection Failure Detection: After the cyclic strain of the test devices, one failed sample (failure in interconnection) per ink–adhesive combination was selected for more detailed evaluation by cross-sectional imaging. To make the cross sections, a broad ion beam (BIB) method using 4 kV argon ions was used for milling to have the least possible damage to the selected samples. Afterward, the cross sections were imaged using a scanning electron microscope (SEM) to gain deep insights into the pad-to-footprint failure mechanisms.

Supporting Information

Supporting Information is available from the Wiley Online Library or from the author.

Acknowledgements

Conflict of Interest

The authors declare no conflict of interest.

Data Availability Statement

Research data are not shared.

Keywords

[1] D. Gräf, J. Franke, N. Ischdonat, M. Hedges, J. Hörber, in *2017 21st European Microelectronics and Packaging Conf. (EMPC) Exhibition*, Warsaw, Poland **2017**, pp. 1–6.

[2] N. Ischdonat, C. Dreyer, D. Gräf, J. Franke, J. Hörber, M. Hedges, in *2018 13th Int. Congress Molded Interconnect Devices (MID)*, Würzburg, Germany **2018**, pp. 1–5.

[3] *OE-A Roadmap for Organic and Printed Electronics*, VDMA Verlag, **2017** edition.

[4] Y. Khan, A. Thielens, S. Muin, J. Ting, C. Baumbauer, A. C. Arias, *Adv. Mater.* **2020**, *32*, 1905279.

[5] J. S. Chang, A. F. Facchetti, R. Reuss, *IEEE J. Emerging Sel. Top. Circuits Syst.* **2017**, *7*, 7.

[6] S. Khan, N. Yogeswaran, W. Taube, L. Lorenzelli, R. Dahiya, *J. Micromech. Microeng.* **2015**, *25*, 125019.

[7] B. S. Cook, J. R. Cooper, M. M. Tentzeris, *IEEE Microwave Wireless Compon. Lett.* **2013**, *23*, 353.

[8] Y. Chu, C. Qian, P. Chahal, C. Cao, *Adv. Sci.* **2019**, *6*, 1801653.

[9] S. Stalf, *IEEE Trans. Consum. Electron.* **2001**, *47*, 426.

[10] S. Chung, K. Cho, T. Lee, *Adv. Sci.* **2019**, *6*, 1801445.

[11] G.-J. N. Wang, A. Gasperini, Z. Bao, *Adv. Electron. Mater.* **2018**, *4*, 1700429.

[12] C. Sternkiker, E. Sowade, K. Y. Mitra, R. Zichner, R. R. Baumann, *IEEE Trans. Electron Devices* **2016**, *63*, 426.

[13] G. A. Torres Sevilla, M. M. Hussain, *IEEE J. Emerging Sel. Top. Circuits Syst.* **2017**, *7*, 147.

[14] E. Torres Alonso, D. P. Rodrigues, M. Khetani, D.-W. Shin, A. De Sanctis, H. Joulie, I. de Schrijver, A. Baldycheva, H. Alves, A. I. S. Neves, S. Russo, M. F. Craciun, *npj Flexible Electron.* **2018**, *2*, 1.

[15] K. Keränen, P. Korhonen, J. Rekilä, O. Tapaninen, T. Happonen, P. Makkonen, K. Rönkä, *Int. J. Adv. Manuf. Technol.* **2015**, *81*, 529.

[16] D. Mager, A. Peter, L. D. Tin, E. Fischer, P. J. Smith, J. Hennig, J. G. Korvink, *IEEE Trans. Med. Imaging* **2010**, *29*, 482.

[17] E. Bihar, S. Wustoni, A. M. Pappa, K. N. Salama, D. Baran, S. Inal, *npj Flexible Electron.* **2018**, *2*, 1.

[18] Y.-S. Huang, K.-Y. Chen, Y.-T. Cheng, C.-K. Lee, H.-E. Tsai, *IEEE Electron Device Lett.* **2020**, *41*, 597.

[19] L. M. Ferrari, U. Ismailov, J.-M. Badier, F. Greco, E. Ismailova, *npj Flexible Electron.* **2020**, *4*, 1.

[20] R. Herbert, S. Mishra, H.-R. Lim, H. Yoo, W.-H. Yeo, *Adv. Sci.* **2019**, *6*, 1901034.

[21] J. Kim, P. Gutruf, A. M. Chiarelli, S. Y. Heo, K. Cho, Z. Xie, A. Banks, S. Han, K.-I. Jang, J. W. Lee, K.-T. Lee, X. Feng, Y. Huang, M. Fabiani, G. Gratton, U. Paik, J. A. Rogers, *Adv. Funct. Mater.* **2017**, *27*, 1604373.

[22] S. Xu, Y. Zhang, L. Jia, K. E. Mathewson, K.-I. Jang, J. Kim, H. Fu, X. Huang, P. Chava, R. Wang, S. Bhole, L. Wang, Y. J. Na, Y. Guan, M. Flavin, Z. Han, Y. Huang, J. A. Rogers, *Science* **2014**, *344*, 70.

[23] T. Vuorinen, K. Noponen, A. Vehkaoja, T. Onnia, E. Laakso, S. Leppänen, K. Mansikkamäki, T. Seppänen, M. Mäntysalo, *Adv. Mater. Technol.* **2019**, *4*, 1900246.

[24] D. Pani, A. Achilli, A. Spanu, A. Bonfiglio, M. Gazzoni, A. Botter, *IEEE Trans. Neural Syst. Rehabil. Eng.* **2019**, *27*, 1370.

[25] H. Kim, Y.-S. Kim, M. Mahmood, S. Kwon, N. Zavanelli, H. S. Kim, Y. S. Rim, F. Epps, W.-H. Yeo, *Adv. Sci.* **2020**, *7*, 2000810.

[26] A. Kaidarova, M. A. Khan, M. Marengo, L. Swanepoel, A. Przybysz, C. Muller, A. Fahlman, U. Buttner, N. R. Geraldi, R. P. Wilson, C. M. Duarte, J. Kosel, *npj Flexible Electron.* **2019**, *3*, 1.

[27] Y. Wei, K. Yang, M. Browne, L. Bostan, P. Worsley, *IEEE Sens. Lett.* **2019**, *3*, 1.

[28] J. Reboun, S. Pretl, J. Navratil, J. Hlina, in *2016 39th Int. Spring Seminar on Electronics Technology (ISSE)*, Pilsen, Czech Republic **2016**, pp. 184–188.

[29] T. Happonen, T. Ritvonen, P. Korhonen, J. Häkkinen, T. Fabritius, *Int. J. Adv. Manuf. Technol.* **2016**, *82*, 1663.

[30] T. Happonen, T. Ritvonen, P. Korhonen, J. Häkkinen, T. Fabritius, *IEEE Trans. Device Mater. Reliab.* **2016**, *16*, 25.

[31] J. F. J. M. Caers, H. De Vries, X. J. Zhao, E. H. Wong, *J. Semicond. Technol. Sci.* **2003**, *3*, 122.

[32] T. Happonen, J.-V. Voutilainen, T. Fabritius, *IEEE Trans. Device Mater. Reliab.* **2014**, *14*, 1005.

[33] N. Palavesam, D. Bonfert, W. Hell, C. Landesberger, H. Gieser, C. Kutter, K. Bock, in *2016 IEEE 66th Electronic Components and Technology Conf. (ECTC)*, IEEE, Las Vegas, United States **2016**, pp. 1664–1670.

[34] T. Happonen, T. Kokko, E. Juntunen, K. Rönkä, *Flexible Printed Electron.* **2019**, *4*, 025002.

[35] S. Gupta, W. T. Navaraj, L. Lorenzelli, R. Dahiya, *npj Flexible Electron.* **2018**, *2*, 1.

[36] A. J. Gallagher, A. N. Anniadh, K. Bruyère, M. Otténio, H. Xie, M. D. Gilchrist, *Dynamic Tensile Properties of Human Skin*, can be found under/paper/Dynamic-Tensile-Properties-of-Human-Skin-Gallagher-Anniadh/55483b16cf13a945a44abe114202d08b865be76b, **2012**.

[37] B. Huyghe, H. Rogier, J. Vanfleteren, F. Axisa, *IEEE Trans. Adv. Packag.* **2008**, *31*, 802.

[38] R. Gomatam, K. L. Mittal, *Electrically Conductive Adhesives*, CRC Press, Boca Raton **2008**.

[39] P. Savolainen, *Failure Modes in Conductive Adhesives*, https://www.dfrsolutions.com/failure-modes-in-conductive-adhesives, (accessed: April 2020).

[40] M. Chin, J. R. Barber, S. J. Hu, *IEEE Trans. Compon. Packag. Technol.* **2006**, *29*, 137.

[41] M. Mosallaei, J. Jokinen, M. Honkanen, P. Iso-Ketola, M. Vippola, J. Vanhala, M. Kanerva, M. Mäntysalo, *IEEE Trans. Compon. Packag. Manuf. Technol.* **2018**, *8*, 1344.